EES Catalysis

PAPER

View Article Online
View Journal | View Issue

Cite this: *EES Catal.*, 2024, 2, 647

Non-thermal plasma catalysis driven sustainable pyrolysis oil upgrading to jet fuel under near-ambient conditions†

Hoang M. Nguyen, Ali Omidkar, Wenping Li, Zhaofei Li and Hua Song *

Received 16th December 2023,
Accepted 30th December 2023

DOI: 10.1039/d3ey00309d

rsc.li/eescatalysis

The global aviation industry is under increasing pressure to mitigate its environmental impact and achieve net-zero objectives. Reducing CO_2 emissions alone is insufficient, as it overlooks crucial parts of the overall climate impacts. Addressing climate-neutral aviation fuel production from sustainable feedstock and effective technology is crucial. Here, we present a breakthrough in sustainable upgrading of pyrolysis oil with CH_4 to jet fuel using non-thermal plasma triphase catalysis, characterized by an opposite gas–liquid flow and a fluidized catalyst under near-ambient conditions of atmospheric pressure and around 100 °C, resulting in an impressive liquid oil yield of almost 87%. This work delves into the strategic distribution of iridium (Ir) as minute nanoclusters on GaN, which serves to ensure robust catalytic stability and instigate synergistic interactions between plasma and catalysis. This unique configuration establishes an active surface conducive to the transformation of pyrolysis oil into essential jet fuel constituents, encompassing gasoline hydrocarbons (C_5–C_{11}), aromatics, and cycloalkanes. Both empirical experiments and computational analysis converge to confirm that methane activation can effectively occur within the plasma zone while surface reactions of cleavage of C–H, C–O, and C–N bonds with adsorbed H and CH_x active species occurring on the Ir(100) surface play a crucial role in enhancing selectivity, resulting in upgraded oil meeting jet fuel commercial specifications. This novel approach holds substantial promise in the pursuit of sustainable and eco-friendly jet fuel production.

Broader context

In the global pursuit of combating climate change and advancing sustainability, the transportation industry emerges as a substantial contributor to carbon emissions. As the urgency of addressing environmental concerns intensifies, the spotlight has increasingly turned towards sustainable fuel production from renewable sources with novel technologies, offering a pivotal avenue for mitigating environmental footprints. Our research marks a significant stride in the realm of fuel production powered by non-thermal plasma catalysis under ambient pressure and low-temperature conditions. Through the innovative integration of non-thermal plasma catalysis, featuring nanoclustered iridium supported on gallium nitride, we have unlocked a groundbreaking approach for converting pyrolysis oil into jet fuels with natural gas (CH_4) in a triphase system characterized by CH_4 gas, liquid oil, and fluidized catalyst particles. This pioneering method operates under mild conditions, yielding an 87% liquid oil output while rigorously meeting the demanding specifications of aviation fuels. The synergy of the nanoclustered iridium catalyst and energetic electrons injects a transformative element into our work. Both empirical data and computational modeling unequivocally affirm the pivotal role of plasma in effectively activating methane and generating active species, notably H^* and CH_x^*, which facilitate the cleavage of long-chain oil molecules on the highly active nanoclustered iridium surface. Beyond the fuel sector, our findings ripple into the broader landscape of sustainable energy or chemical production powered by plasma catalysis.

1. Introduction

At the beginning of the 2020s, global concerns over energy insecurity, climate change, and mounting agricultural waste prompted the adoption of biofuels as renewable alternatives in countries worldwide. The depletion of fossil fuel reserves and the urgent need to address climate change have accelerated the pursuit of sustainable energy solutions in various sectors. Among these sectors, the aviation industry, a major contributor to greenhouse gas emissions, faces significant challenges in transitioning to greener alternatives. In 2018 alone, the aviation sector consumed approximately 94 billion gallons of jet fuels worldwide.[1] The demand for jet fuels has seen substantial growth in recent years due to the expansion of air travel and

Green Catalysis Research Group, Department of Chemical and Petroleum Engineering, University of Calgary, 2500 University Dr NW, Calgary, AB T2N 1N4, Canada. E-mail: sonh@ucalgary.ca

† Electronic supplementary information (ESI) available. See DOI: https://doi.org/10.1039/d3ey00309d

the increasing number of commercial flights. The European Commission recognizes the importance of policies that address the complete climate impacts of aviation[2] as indicated in their acknowledgement of the need for such measures. In the ''Destination 2050'' roadmap, aircraft manufacturers, airports, and airlines based in the European Union have set a target to reduce CO_2 emissions by 92% by the year 2050.[3] Many regions and countries have also followed a similar approach. The focus has long been on mitigation strategies involving enhancing air traffic management, developing larger and more fuel-efficient aircraft, promoting the use of sustainable aviation fuels, and implementing measures to offset any remaining effects. The aviation industry plays a significant role in global energy consumption and carbon emissions, necessitating a shift toward more sustainable fuel options. The development of renewable jet fuels that are compatible with existing aircraft engines is crucial for achieving a more sustainable aviation sector.

There are pathways certified by the American Society for Testing and Materials (ASTM) for jet fuel production, including gas-to-jet (GTJ) such as Fischer–Tropsch synthesis (FTS), oil-to-jet (OTJ) such as hydrotreated renewable jet (HRJ), alcohol-to-jet (ATJ) such as ethanol-to-jet or butanol-to-jet, and sugar-to-jet (STG) such as catalytic upgrading of sugar to jet.[4] However, of all the ASTM-certified options, only hydroprocessed esters and fatty acids (HEFA bio-jet), also known as HRJ, have reached a mature stage and are currently being commercially developed to produce drop-in biofuels.[5] Bio-jet fuel, obtained from esters and fatty acids sourced from various materials, including oilseed crops, algae, and oils, fats, and greases, faces the challenge of a high feedstock cost, which constitutes about 80% of the total bio-jet production cost, even though triglyceride-based oils are easier to convert into liquid fuels compared to starch and cellulose.[6] In contrast, the abundant renewable resource of lignocellulosic biomass, which yields approximately 150 to 170×10^9 tons annually,[7] holds promise as a cost-effective feedstock for advanced biofuel production, offering potentially reduced or even neutral environmental impacts. Pyrolysis oil to jet fuel production uses renewable feedstocks like biomass, agricultural residues, or waste materials, which are plentiful and eco-friendly, reducing dependence on fossil fuels. Nonetheless, pyrolysis oil requires more extensive upgrading compared to oils from hydrothermal liquefaction given its high oxygen content, low heating value, poor thermal stability, acidity, chemical instability, corrosiveness, and immiscibility with petroleum.[8]

The debate revolves not so much only around the sustainability of the feedstocks but rather its level of technological advancement. It remains unclear from the available literature that which pathway offers superior overall economic feasibility. This suggests that the fuel must be produced using what is known as second-generation technology. Upgrading pyrolysis oil to hydrocarbon fuels under mild conditions (low temperature and low hydrogen pressure) by conventional catalytic thermal processes presents a significant challenge due to the high dissociation energy required to cleave perdurable bonds such as C–H (4.3 eV)[9] and aromatic C–O bonds, which is approximately 4.8 eV.[10] In general, the disruption of these stable bonds typically requires elevated temperatures exceeding 350 °C. However, this often gives rise to undesired outcomes like char or tar formation, as well as catalyst deactivation, imposing significant constraints on the reaction processes.[11] Traditional hydrotreating processes for pyrolysis oil also require high and pure H_2 pressures (>100 bars) in the presence of a catalyst,[12] resulting in a product with a significant portion of hydrogen and approximately 20% by weight of liquid hydrocarbons, suitable for the direct use as gasoline and jet fuels.[13] An alternative approach, fluid catalytic cracking, involves a single stage of hydrotreatment followed by fluid catalytic cracking using a zeolite as a catalyst,[14] but this method is less commonly used for producing transportation fuels and primarily yields commodity chemicals.[15] The utilization of pure H_2 for chemical processes is considered economically and environmentally unsustainable.[16] More importantly, the primary method for hydrogen production involves the energy-intensive reforming of natural gas.[17] Leveraging CH_4 directly as an active H_2 source has the potential to substantially lower operational expenses and decrease greenhouse gas emissions.[16] Non-thermal plasma (NTP) catalysis emerges as a viable technique for dissociating hydrogen from CH_4 and breaking C–O and C–N bonds in pyrolysis oil under conditions closely approximating ambient parameters, including atmospheric pressure and low temperatures. This process is facilitated by the influence of high-energy electrons, reaching up to 10 eV.[18] NTP offers high reactivity, straightforward on/off, versatile, and a tunable process.[19] Furthermore, NTP relies on electrical energy and can seamlessly integrate into electrification systems fuelled by renewable sources like solar and wind power,[20] with the aim of achieving carbon-neutral jet fuel production. The prospects of plasma catalytic technology for transforming pyrolysis oil into jet fuel are notably more promising in comparison to conventional thermal catalytic processes. However, a notable void exists in the literature regarding the application of NTP for directly upgrading liquid phase pyrolysis oil. The current hurdles within the plasma catalytic pathway encompass the need for a deeper understanding of the intricate interplay between the plasma and the catalyst, even more complicated with in-liquid plasma, as well as the efficient utilization of plasma energy.[16] The successful integration of NTP into the jet fuel production value chain depends on overcoming technical and economic challenges and aligning with the evolving regulatory landscape. Continued research, innovation, and collaboration between academia, industry, and governments will play a crucial role in driving the development and deployment of this emerging technology, ultimately contributing to a more sustainable aviation sector.

In light of insights gleaned from the existing literature[21,22] coupled with our prior experimental observations in plasma-driven methane activation,[19,23,24] two pivotal challenges persist, preventing plasma catalytic processes from completely supplanting conventional thermal heating chemical methodologies. Often disregarded, these challenges encompass: (i) the

in situ plasma-induced decomposition of intended products or excessive hydrogenation of oil, leading to gas production instead of the desired gasoline or aromatics and (ii) the dissipation of energy in the form of emitted photons and heat within the plasma reaction environment. Addressing the former hurdle may involve tailoring the design of catalyst porous structures and the strategic distribution of active centers. Pioneering research studies have indicated this possibility, citing the catalytic ability to shield products within the plasma regime.[25] The second obstacle would be overcome by using a catalyst with photocatalytic properties to adsorb wasted photons to boost the catalytic performance further. Gallium nitride (GaN), a stable wurtzite-structure member of Group III nitrides and a well-known wide bandgap semiconductor with a fundamental bandgap energy of 3.4 eV, has gained significant attention as a revolutionary material due to its exceptional electronic and optical properties.[26] In the realm of catalytic applications, GaN is increasingly being explored as a photocatalyst, thanks to its remarkable chemical and thermal stabilities.[27] Recent research has shown that GaN exhibits catalytic abilities in activating C–H bonds, particularly in the non-oxidative aromatization of light alkanes such as methane, with evidence from a study suggesting a relatively low activation energy for methane coupling on GaN surfaces, where the rate-limiting step is the cleavage of C–H bonds in CH_x species adsorbed on the Ga top site.[28] In addition, Ir has been proven as an excellent active center for dehydrogenation from hydrocarbons and bio-oil.[29,30] Despite significant advancements in the last decade, the development of an Ir catalyst with sufficient mass activity and stability remains a long-term objective, hindered by the challenge of identifying active sites and dealing with adverse reconstruction during operation.[31] The highly effective catalysts would be those that feature smaller particle sizes of metallic Ir on GaN, serving as hybrid catalysts and supports. This configuration would result in enhanced electronic properties, significantly improved plasma interaction, and limited catalyst sintering. To the best of our knowledge, no prior research has reported the use of Ir-based catalysts for plasma-driven pyrolysis oil upgrading to jet fuel in the existing literature. Consequently, we aim to address and bridge this knowledge gap by offering valuable insights into catalyst development and exploring the synergistic effects of plasma and catalysis on the upgrading performance. This work seeks to contribute new perspectives and understanding to the field.

Here, we present synergetic triphase phase catalysis plasma driven pyrolysis oil upgrading to jet fuel with CH_4 as a H donor source under mild conditions of atmospheric pressure and low temperature of approximately 100 ± 5 °C. We use Ir supported on GaN as an active catalyst for CH_4 activation to provide active species for the cleavage of C–H, C–N, and C–O bonds of oil molecules, and we propound that GaN with photocatalytic properties can use wasted photons induced in the plasma regime to promote the upgrading performance further. To initiate our investigation, we focused on devising a suitable support architecture essential for stabilizing the active Ir component. We infer that the agglomeration of large nanoparticles involves surface migration and coalescence; to prepare an Ir nanocluster catalyst, we therefore interfere these two steps by inducing a N-ligand to limit the fusion of Ir clusters to larger particle sizes. These ligands are considered essential for providing stability and influencing the electronic properties of mononuclear active sites through covalent bonding with the Ir metal centers and ligands. This understanding underscores the significance of designing a support material with electron-donating functional groups on its surface, mimicking the characteristics of a mononuclear Ir pincer complex. This design element stands as a pivotal factor in the advancement of an Ir-based nanocluster for plasma driven oil upgrading. Synergistic effects between clustered Ir and plasma lead to the formation of mobile electrons for CH_4 activation and cleavage of heavy oil molecules to lighter components. The majority of the upgraded oil properties align with the ASTM standard for engine jet fuel with an excellent stability attributed to plasma-catalytic synergism. The observed outcomes lay the foundation for pioneering pathways in sustainable fuel production, promising novel routes for advancements within the field.

2. Experimental

2.1. Catalyst preparation

Ir/GaN catalysts were prepared by using a wet impregnation method with the assistance of 2-methylimidazole (99%, Sigma Aldrich) as a surface ligand to enable a cluster of Ir particles. In this study, three different catalyst loadings, 0.01%, 0.05%, and 0.1 wt% of Ir, were prepared. The use of such low Ir loadings serves the dual purpose of preventing potential agglomeration of Ir particles during synthesis, thereby inhibiting the formation of larger particles. Additionally, the approach ensures cost-effectiveness. This low catalyst loading strategy aligns with principles of efficiency and economy by optimizing the utilization of the catalyst, particularly one containing the precious metal Ir. It also minimizes the risk of saturation of active sites, enhancing selectivity while promoting the synergistic effects between the plasma and the catalyst for overall reaction efficiency. Furthermore, this practice adheres to green chemistry principles, reducing waste and considering the environmental impact. 2-Methylimidazole has been used as a genetic modulator to fine-tune ligands at the Co(II) center, inducing a self-adaptive coordination state for Co(II).[32] In this work, 2 g of 2-methylimidazole was added into the deionized water and stirred at 500 rpm for 2 h at room temperature. Iridium(III) chloride (99.8%, Sigma-Aldrich) was weighted accurately and transferred to the mixing solution. The precursor solution was mixed at 500 rpm for 24 h at 60 °C. The pH of the solution diminished from 6.2 to 5.6, indicating the release of HCl from the reaction between $IrCl_3$ and 2-methylimidazole. Gallium mononitride (GaN, 99.9%, Sigma Aldrich) was weighted accurately and added to the mixing solution. We expected that the unshared pair of electrons located on the nitrogen atom in 2-methylimidazole can readily rival the coordination effects of acids, impacting the iridium crystal's nucleation and growth.

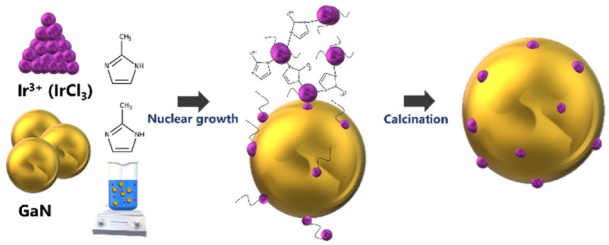

Fig. 1 Schematic diagram of the synthesis process for the nanocluster Ir/GaN catalyst.

The presence of N-ligand enables the creation of numerous well-distributed iridium active sites with an iron atomic cluster (Fig. 1). This addresses the limitations of conventional plasma materials, which have fewer active sites and an uneven distribution. The lone pair of electrons on the nitrogen atom in 2-methylimidazole plays a pivotal role in stabilizing the cluster formation during its growth, contributing to the overall stability of the structure. However, it is important to note that during the subsequent calcination process, these ligands are expected to be removed. The calcination step is anticipated to eliminate the ligands, allowing the formation of the final cluster structure with the desired electronic properties. The dried catalyst precursor was calcined in a furnace by using a tube furnace at 500 °C for 4 h at a heating rate of 10 °C min^{-1} in air prior to further treatment in a tube furnace with a 5% H_2/Ar mixture at 500 °C for 4 h at a heating rate of 3 °C min^{-1}.

2.2. Catalyst characterization

2.2.1. XRD. The crystalline structure of the prepared catalyst was evaluated by X-ray diffraction (XRD) using a Rigaku ULTIMA III X-ray diffractometer. The Cu Kα radiation source was operated at 40 kV and 44 mA. Scans were obtained within a 2θ range of 10 to 60° at a rate of 2° per minute.

2.2.2. N_2 adsorption–desorption isotherms. The catalysts underwent N_2 adsorption analysis utilizing a Micromeritics ASAP 2020 Plus surface area and porosimeter system. The sample was subjected to degassing at 350 °C for 4 h, at a temperature ramping rate of 10 °C per minute and a vacuum level of 10 mmHg. Liquid nitrogen was used for the analysis, resulting in a 28-point adsorption isotherm. The total surface area was determined using the Brunauer, Emmett and Teller (BET) method, while the total pore volume was ascertained at a relative pressure of 0.995.

2.2.3. Ammonia temperature programmed desorption (NH_3-TPD). NH_3-TPD experiments were undertaken to examine the acidity of the prepared catalyst, utilizing a Micromeritics AutoChem II 2920 chemisorption analyzer. Ammonia was selected as a probe molecule due to its uncomplicated nature, small molecular size, and capacity to evaluate both robust and weak acid sites within the catalyst. Prior to each measurement, a fresh sample weighing 0.2 g underwent pretreatment with pure helium (He) at 600 °C at a ramp rate of 10 °C per minute. This pretreatment was followed by a 10-minute hold under a He flow rate of 25 cm^3 per minute. The desorption of ammonia was quantified using a meticulously calibrated thermal conductivity detector (TCD). This analysis established a direct link to the ammonia production reaction under study, thereby validating the interaction between ammonia and the catalyst.

2.2.4. CO pulse chemisorption. CO pulse chemisorption experiments were conducted by using a Micromeritics AutoChem II 2920 chemisorption analyzer. These experiments were carried out under a helium flow of 20 mL min^{-1}, serving as the carrier gas. Approximately 100–150 mg of each catalyst was securely placed between quartz wool within a quartz reactor assembly situated inside a furnace. The temperature at the sample location was precisely monitored using a K-type thermocouple enclosed in a quartz capillary. To ensure the reliability of the results, all samples underwent thermal pretreatment with a mixture of 5% H_2/Ar to eliminate potential surface contamination. Such contamination might arise from the adsorption of unwanted molecules, including carbon species or water present in the atmosphere. The pulse chemisorption was executed at a constant temperature of 400 °C with a linear increase of 10 °C min^{-1}. In pulse chemisorption, the consumption of CO and in TPD was monitored using a thermal conductivity detector. In this setup, CO molecules were transported by the carrier gas to a thermal conductivity detector, which measured the signal difference between the desorbed gas and a reference flow.

2.2.5. Thermogravimetric analysis (TGA). The amount of carbon formation was quantified by using TGA. The solid products underwent meticulous drying in an oven maintained at 110 °C. TGA measurements were executed utilizing a simultaneous thermal analyzer (PerkinElmer STA 6000). Initially, the samples were stabilized at 30 °C for 5 minutes to establish their initial weight. They were subsequently subjected to a gradual temperature rise, reaching up to 800 °C at a rate of 20 °C min^{-1}. This process was conducted under a continuous air flow of 30 mL $minute^{-1}$, and the samples were maintained at 800 °C for 5 mins. The weight reduction noted within the temperature range of 350 °C to 800 °C was attributed to the oxidation of coke. The mass of coke was computed based on the assumption that it was uniformly distributed across the catalyst.

2.2.6. X-ray photoelectron spectroscopy (XPS). Room-temperature XPS experiments were performed using a Kratos Axis spectrometer, equipped with monochromatized Al Kα ($h\nu$ = 1486.71 eV) radiation. Calibration of the spectrometer was accomplished using the Au $4f_{7/2}$ binding energy (84.0 eV) with reference to the Fermi level. Experiments were performed under a vacuum pressure higher than 5×10^{-10} torr within the analysis chamber. Core-level spectra were acquired using a hemispherical electron-energy analyzer set to a pass energy of 20 eV. A survey spectrum spanning binding energies from 0 to 1100 eV was collected with an analyzer pass energy of 160 eV. Charge effects were rectified using a C_{1s} peak at 284.8 eV, while a Shirley background subtraction was applied to mitigate inelastic background effects in core-level peaks. To extract accurate peak parameters like positions, widths, and intensities, a nonlinear optimization approach employing the Marquardt Algorithm (Casa XPS) was adopted for curve fitting. The

core-level lines in XPS were modeled using a Gaussian–Lorentzian composite peak function. Ultraviolet photoelectron spectroscopy (UPS) measurements were conducted using a He I source ($h\nu$ = 21.2 eV), with the sample held at a bias of −10 V. UPS was powered at 3 kV × 20 mA (60 W). Compositional analyses were determined from survey spectra using major elemental peaks and sensitivity factors obtained from the database.

2.2.7. Scanning transmission electron microscopy-energy-dispersive X-ray spectroscopy (STEM-EDX). STEM analysis was performed using an FEI Tecnai F20 system with a field emission gun (FEG) operating at 200 kV, accompanied by a 4k Gatan CCD camera. For this analysis, approximately 0.05 g of the catalyst was initially dispersed in ethanol and then supported on holey carbon placed on a 200 mesh Cu grid. The resulting STEM images were subsequently captured. High-resolution transmission electron microscopy (HRTEM) images were acquired for the fresh and spent Ir/GaN samples. This analysis took place on the FEI Talos F200X, high-resolution scanning/transmission electron microscopy operation within the range of 80 to 200 kV. The microscope was equipped with a high-angle annular dark field (HAADF) detector for *Z* contrast imaging and a Super X-EDX detector for compositional analysis.

2.3. Evaluation of plasma catalytic performance

The experimental setup is depicted in Fig. S1 (ESI†). The oil upgrading reaction was conducted in a dielectric barrier discharge (DBD) reactor constructed from a quartz tube (an inner diameter of 8 mm, an outer diameter of 10 mm, and a thickness of 1 mm) with a coaxial stainless steel rod electrode (4 mm diameter) positioned at the center of the quartz tube and grounded with a silver mesh. For each trial, 0.1 g of catalysts (GaN and Ir/GaN) in a finely powdered form was packed at the reactor's core. The catalyst bed was secured using a quartz fritz with porosity #4, enabling gas passage. Prior to each experiment involving the catalyst, we commenced by introducing 0.1 cm^3 of biomass-derived pyrolysis oil (supplied by FORGE Hydrocarbons Corp, Canada) to moisten the catalyst layer, followed by the introduction of CH_4 gas to initiate the fluidized bed. Plasma was generated using a LEAP100© plasma generator with a maximum power of 700 W and an applied voltage of up to 80 kV_{pk-pk}. The catalytic performance assessment was conducted at 12 W. To optimize mass transfer efficiency and product purity, a counter-current flow technique was employed, where CH_4 gas and liquid oil were introduced in opposite directions. CH_4 (ultra high purity, 99.99%, ALPHAGAZTM 1, Canada) was fed into the reactor from the bottom at a flow rate of 100 cm^3 min^{-1}, while pyrolysis oil was introduced from the top downward at a flow rate of 0.05 cm^3 min^{-1} using a high-precision, high-pressure piston pump (Masterflex®). This configuration was used to enable the good mass transfer and prevent the liquid oil condensed in the reactor. This study included a control experiment in which the reaction was carried out using an external thermal heater set at 100 ± 5 °C to assess the impact of conventional thermal effects on the upgrading performance. However, no CH_4 conversions or improvements in oil properties under these test conditions were observed, indicating that the influence of thermal factors on the reaction performance was effectively mitigated. For the plasma reaction test, the emitted light from the plasma reactor was analyzed using an optical system to provide *in situ* insights into the plasma reaction. Emission spectra from the glow region were captured at the reactor center. The measurements were recorded using a single-channel UV-VIS-NIR spectrophotometer in the scope mode (Avantes Inc., USB2000 Series) with a 400 μm fiber optic cable. The spectral range covered 200 to 800 nm, employing a line grating of 600 lines per mm and a 0.4 nm resolution. The temperature of the reactor was monitored using an infrared thermal camera (Flir©). Accurately measuring the temperature of the catalyst surface within the plasma reactor presents a challenging endeavor due to the intricate interactions involving high-energy electrons and plasma species. The measured temperature pertains to the external surface of the plasma reactor, serving as reference values for reproducible experiments and facilitating an assessment of the temperature effects on plasma catalytic reactions.

2.4. Product analysis

2.4.1. Gas analysis. Gas analysis was carried out by using micro-gas chromatography (GC) (Agilent © 490), which was capable of analyzing various gases including H_2, N_2, O_2, CO, CO_2, CH_4, C_2H_4, C_2H_6, C_2H_4, C_2H_6, C_2H_4, C_3H_6, C_3H_8, C_4H_8, C_4H_{10}, C_5H_{10}, and C_5H_{12}. Details regarding gas conversion and product yield calculations are provided in the ESI.†

2.4.2. Liquid analysis. Upgraded oil products were collected using a condenser at approximately 5 °C and analyzed by gas chromatography-mass spectroscopy (GC-MS, PerkinElmer GC Claus 680 and MS Clarus SQ 8 T). The GC-MS was equipped with a Paraffins-Olefins-Naphthenes-Aromatics (PONA) column (Agilent HP-PONA). The mass detector was configured to scan the *m*/*z* range from 10 to 400. Compounds were identified by comparing the detected mass spectra with those in the built-in National Institute of Standards and Technology (NIST) database of the system.

2.4.3. Molecular weight assessment of upgraded oil. To evaluate the boiling point variation and estimate the average molecular weight, feedstock and product oil samples underwent simulated distillation analysis. This analysis was performed using an Agilent 8890 GC System equipped with the SimDis Expert analysis software developed by separation systems. The GC analysis was carried out under cryogenic conditions using liquid nitrogen, spanning from −20 °C to 425 °C at a ramp rate of 10 °C min^{-1}. Boiling curves were calibrated utilizing the reference sample SD-SS3E-05 provided by separation systems. Subsequently, the average molecular weights of feedstock and products were calculated based on these simulated distillation curves.

2.4.4. Total acid number (TAN). The TAN was used to characterize the acidity of feed and product oil, using a Metrohm 848 Titrino Plus titrator. Typically, the sample was dispersed in a titration solution containing 50 wt% toluene, 49.5 wt% 1-propanol, and 0.5 wt% water. An automatic and continuous addition of 0.1 mol L^{-1} KOH was performed until a sudden change in electrode potential was observed. The TAN

value was then calculated based on the volume of KOH solution consumed during the titration process.

2.4.5. Density and viscosity analysis. The density of the liquid product was measured at around 15 ± 0.5 °C using an Anton Paar DMA 4500M density analyzer, with each measurement repeated three times for an average result. Oil viscosity was determined using a Fungi-designed viscometer equipped with an L-series viscometer and a PolyScience LS 51 compact cycle refrigerator to ensure that measurements were taken at 15 ± 0.5 °C.

2.5. Computational details

To determine optimized geometric configurations, the Dmol3 code integrated within the Material Studio package (Accelrys, San Diego, CA) was employed. The software utilizes the Perdew–Burke–Ernzerhof (PBE) functional method within the generalized gradient approximation (GGA) framework to effectively explore electron exchange and correlation interactions within crystal-based materials interacting with small gas molecules. The ''DFT-D of Grimme'' algorithm was employed to accurately account for van der Waals interactions, which significantly influence physisorption processes. By conducting Monte Carlo simulations across the substrate–adsorbate system's configurational space, the BIOVIA Materials Studio Adsorption Locator identifies potential adsorption arrangements as the temperature is gradually reduced by simulated annealing. This iterative process aids in identifying local energy minima. In most instances, adsorbates are molecular gases or liquids, whereas substrates typically encompass solid surfaces (crystalline or amorphous), porous materials, or substantial molecules (such as carbon nanotubes or nanocatalysts). The initial step in depicting the methane activation process on the Ir–GaN catalyst involves identifying the active site responsible for methane activation. This determination is made by evaluating the adsorption energy using eqn (1). The gallium nitride surface (GaN(110)) was chosen to represent the substrate, while the active metal nanocluster (Ir(100)) loaded onto this support was selected as the catalytic entity. Subsequently, the system's energy was recalibrated considering the dehydrogenation of methane within a plasma environment. Eqn (2) is employed to investigate the influence of plasma on the catalytic system and reevaluate its energy dynamics.

$$E_{ads} = E_{sur+CH_4} - E_{sur} - E_{CH_4} \quad (1)$$

$$E_{ads} = E_{sur+CH+H} - E_{sur} - E_{CH_4} - E_{H} \quad (2)$$

To elucidate the influence of plasma on methane activation within the catalytic system, we propose the exploration of four distinct reactions (eqn (3)–(6)).

$$CH_4 + e^- \rightarrow CH_3^* + H^* + e^- \quad (3)$$

$$CH_4 + e^- \rightarrow CH_2^* + 2H^* + e^- \quad (4)$$

$$CH_4 + e^- \rightarrow CH^* + 3H^* + e^- \quad (5)$$

$$CH_4 + e^- \rightarrow C + 4H^* + e^- \quad (6)$$

This approach facilitates a comprehensive assessment. Moreover, we also investigated two extra key scenarios: (i) methane adsorption on both GaN and Ir surfaces and (ii) adsorption of CH and H radicals (generated in the plasma) on the GaN and Ir surfaces. By scrutinizing these scenarios, we aim to gain insights into the interplay between plasma and the catalytic methane dissociation.

3. Results and discussion

3.1. Catalyst characterization

The screening test involving plasma-driven pyrolysis oil with different loadings of Ir on GaN revealed notable variations in performance. Specifically, 0.01 wt% Ir/GaN and 0.05 wt% Ir/GaN exhibited lower efficiency compared to 0.1 wt% Ir/GaN (Fig. S2 and S3, ESI†). The diminished performance at lower Ir loadings suggests an insufficient influence on upgrading capabilities, while higher loadings of noble metals may contradict principles of efficiency and economy. The chosen 0.1 wt% Ir/GaN loading strikes a balance, optimizing catalyst utilization and minimizing the risk of active site saturation. This deliberate approach enhances selectivity and facilitates synergistic effects between plasma and the catalyst, contributing to overall reaction efficiency. The subsequent thorough characterization of the optimal 0.1 wt% Ir/GaN catalyst underscores our commitment to methodical investigation and informed catalyst design in this work.

3.1.1. Physico-chemical properties of the catalysts. We initially investigate the physico-chemical properties of Ir/GaN nanocluster catalysts and establish correlations between their structure and the subsequent performance in plasma-driven oil upgrading. The XRD pattern of the GaN sample peaks at 2θ of 19.0°, 24.7°, 30.4°, 32°, 32.7°, 34.8°, 35.5°, 37.2°, 38.7°, 43.5°, 46.12°, 48.4°, 54.8°, and 58.1°, as shown in Fig. 2a. Although the observed diffraction peaks slightly diverged from those reported in the literature for GaN synthesized from its precursor solution, it is important to note that the GaN utilized in our study, obtained from Sigma Aldrich with a purity of 99.9%, provided convincing evidence for the assignment of all detected peaks to GaN. Two broad peaks at 24.8° and 36.2° represent for the presence of amorphous β-Ga_2O_3 while amorphous α-Ga_2O_3 was detected by the diffraction peak at 41.7° 33 from the fresh and spent Ir/GaN catalysts. Interestingly, Liu *et al.*[34] reported observing diffraction peaks of Ir nanoclusters, ranging in size from 2 to 4 nm, supported on graphite at 2θ values of 40.7° and 47.3°. Nonetheless, neither the fresh nor the spent Ir/GaN samples displayed any detectable diffraction peaks related to Ir, indicating a smaller particle size distribution of Ir on the GaN support.

The results of the N_2 adsorption and desorption experiment (Fig. 2b) provided confirmation of the existence of Ir with a small particle size. This was evident from the notable increase in the Brunauer–Emmett–Teller (BET) surface area of the fresh Ir/GaN sample compared to that of the GaN sample. The measured BET specific surface area of GaN was 8.0 $m^2\ g^{-1}$

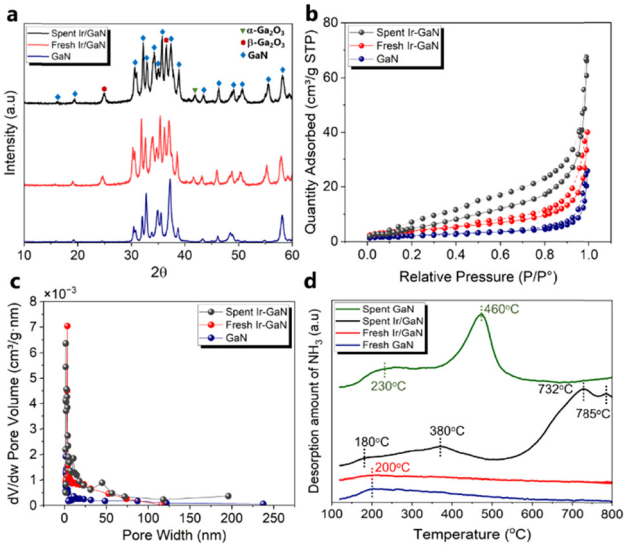

Fig. 2 (a) XRD patterns of the GaN, fresh and spent Ir/GaN catalysts. (b) N_2 adsorption isotherm profiles of the GaN, fresh and spent Ir/GaN catalysts. (c) Pore size distributions of the GaN, fresh and spent Ir/GaN samples. (d) NH_3-TPD profiles of all fresh and spent samples.

with an average corresponding pore size diameter derived from the Barrett–Joyner–Halenda (BJH) method of 19.0 nm and a pore volume of 0.031 $cm^3\ g^{-1}$, as shown in Table S1 (ESI†). The large pore size provided shielding effects for partially dehydrogenated molecules diffused inside such pores[25] to limit a deep dehydrogenation of oil molecule hydrocarbon gas. Incorporating 0.1 wt% of Ir into the GaN led to a rise in the BET surface area and pore volume to 14.6 $m^2\ g^{-1}$ and 0.052 $cm^3\ g^{-1}$, respectively, albeit with a slight decrease in the average pore size to 14.5 nm. These findings suggest that the Ir likely exists in the form of very small particles or nanoclusters, possessing a greater specific surface area than the GaN alone. Additionally, the presence of Ir nanoclusters partially obstructed the mesopores of the GaN, contributing to the observed reduction in pore diameters. Another highly possible reason is that the oxidation of GaN, likely facilitated by Ir, culminates in the production of Ga_2O_3, concurrently inducing the formation of defects and pores. This transformation is discernible through the outcomes of XRD and later TGA. Similar observation of the increment in the BET surface area of α-Fe_2O_3 with the addition of Pd nanocluster[35] ascertains such data interpretation. The larger Type II hysteresis loop observed in the GaN sample confirms the presence of larger surface areas, allowing for the adsorption of molecular clusters around favorable sites on the GaN surface. The pore size distribution analysis of both GaN and fresh Ir/GaN samples reveals a varied pore size distribution, predominantly in the range of 5–20 nm (Fig. 2c). It is noteworthy that the surface area and pore volume of the Ir/GaN catalyst increased after the plasma reaction. Specifically, the BET surface area and pore volume of the spent Ir/GaN catalyst were increased to 23.1 $m^2\ g^{-1}$ and 0.098 $cm^3\ g^{-1}$, respectively. This finding aligns with our earlier assumption regarding the notable stability of the Ir/GaN catalyst, as indicated by the XRD patterns. Many reports on plasma catalysis have noted a decrease in the surface area and pore volume of catalysts after undergoing plasma reactions attributed to catalyst sintering. Our recent observations also indicate minimal sintering of Cu particles after plasma-driven gaseous phase reactions between N_2 and CH_4.[19] The increment in the BET surface area of the spent Ir/GaN catalyst is possibly due to better dispersion of Ir atoms in the nanocluster form in the NTP environment, and in such smaller sizes, catalytic sintering is limited, and plasma discharge during the reaction possibly acted as a surface activation to increase the active surface area.[36]

The catalyst surface acidity plays a crucial role in facilitating dehydrogenation, deoxygenation reactions, and carbon formation. In this work, the surface acidity of the catalyst was assessed using the NH_3-TPD technique, and the results are presented in Fig. 2d. The peak observed at 200 °C is attributed to NH_3 absorption on the weak acid sites (<300 °C) of the GaN support, a consistency with the observations of other researchers.[26] Significantly, the NH_3-TPD profile of the fresh Ir/GaN catalyst exhibits minimal disparity, except for a slight reduction in the desorption peak area compared to that of the GaN. This reduction suggests a slightly lower amount of desorbed NH_3, indicating marginally weaker acidity. This observation implies that Ir exists in the form of nanoclusters or single atoms, confined within the distinctive surface cavities of the GaN. This outcome further substantiates our previous hypothesis regarding the presence of Ir as either single atoms or nanoclusters, as corroborated by the absence of Ir-related XRD peaks in the dispersion of Ir as small particles. Catalysts with weak acidity tend to dissociate hydrogen protons, a trait favorable for dehydrogenation reactions, which leads to the creation of carbon cations serving as precursors for coke formation.[37]

Hence, catalysts displaying weak-to-moderate acidity, coupled with appropriate pore sizes facilitating the removal of coke precursors towards the reaction medium under plasma conditions, provide highly energetic electrons for enhancing the cleavage of C–H and C–O bonds. This combination represents a suitable equilibrium between upgrading performance and resistance to coke formation. Upon analyzing the spent Ir-GaN catalyst, four new peaks emerge at 180, 370, 732, and 785 °C, falling into three acidity regions: weak acidity (120–300 °C), moderate acidity (310–530 °C), and strong acidity (550–800 °C). These novel peaks suggest the formation of fresh acid sites on the catalyst's surface during the reaction.

These new acid sites appear to be more acidic than the weak sites on the fresh Ir/GaN and GaN catalysts but less acidic than the weak sites present on the surface of the initial catalyst. Motivated by this revelation, we conducted the NH_3-TPD characterization of the spent GaN sample, uncovering a novel medium acid site arising from a peak at 460 °C. This newly formed acid site demonstrates greater acidity compared to both the weak and medium sites of the spent Ir/GaN and GaN catalysts. The efficient dispersion of Ir nanoclusters on GaN ensures the preservation of surface acidity without any modification. We firmly believe that alterations in the catalyst

surface acidity are driven by surface restructuring, the redistribution of surface species, and intensified interaction with probe molecules. Plasma treatment has a well-established history as an effective technique for modifying catalyst surfaces. The synergistic interplay between the plasma and the catalyst can lead to the redistribution of surface species, resulting in an increased concentration of acidic sites. Additionally, alterations in surface electron density can influence the adsorption and desorption strength of NH_3, thereby augmenting the observed acidity.

3.1.2. Surface electronic properties of catalysts. To assess the distribution and particle size of Ir on the GaN, we conducted the CO pulse chemisorption characterization over the fresh and spent Ir/GaN and GaN to benchmark the effects of support, and the results are summarized in Fig. 3a. This analysis also underscores the significance of gaining a comprehensive understanding of the interaction between the metal and CO. The obtained CO pulse chemisorption data yield two significant insights. Firstly, there is an absence of detectable CO adsorption on the GaN and spent Ir/GaN samples. This suggests that CO adsorption on Ir-free functionalities is either negligible or falls below our detection limits under the specified experimental conditions. Secondly, there is a gradual decrease in the amount of adsorbed CO up to 70 min, then exhibiting a constant detected CO signal from the fresh Ir/GaN sample. The gradual reduction in the CO adsorption signal observed from 0 to 70 minutes signifies the occurrence of CO adsorption onto the catalyst surface during this interval. This reduction can be attributed to the saturation of active sites on the nanoclusters as they become progressively occupied by adsorbed CO species. Subsequently, a constant signal level was attained after 70 minutes, indicative of an adsorption–desorption equilibrium. This equilibrium reflects a balance between the rate of CO adsorption and desorption, signifying that the nanoclusters' surfaces have reached their maximum CO adsorption capacity under the given experimental conditions. This nuanced behavior offers insights into the kinetics of CO adsorption on nanocluster catalysts and highlights the importance of surface saturation in understanding the catalytic properties of nanoscale materials. It is worth noting that the particle size measured by CO chemisorption for the fresh Ir/GaN sample was determined to be 0.6 nm. However, in the case of the spent Ir/GaN or GaN, accurate measurements were unattainable due to the absence of detected adsorption.

We are convinced that the reactions facilitated by plasma play a pivotal role in the additional decomposition or restructuring of GaN, leading to a significant increase in the surface area (as indicated by the BET surface area results). This process enhances the dispersion of Ir on the surface, and notably, Ir particles were not detectable. In addition, it has been indicated that particle size interpretations obtained through CO chemisorption typically tend to be larger compared to those acquired using XRD and TEM techniques.[38] Even with their superior dispersion and small size, nanoclusters of this magnitude may escape the detection of Ir-related diffraction patterns by XRD. For a more comprehensive understanding of the surface

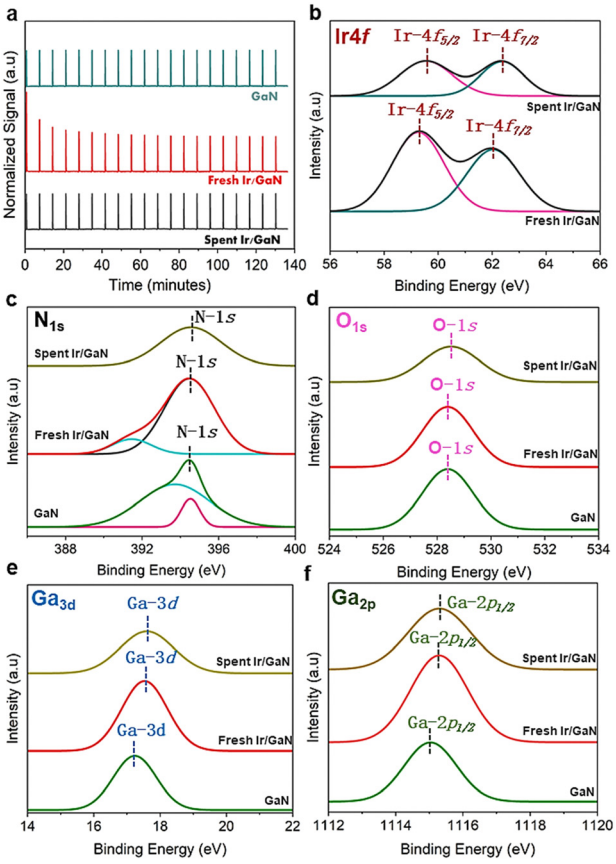

Fig. 3 (a) CO pulse chemisorption profiles of the GaN, fresh and spent Ir/GaN catalysts. (b) High-resolution XPS spectra of the Ir_{4f} and fresh and spent Ir/GaN catalysts. (c) XPS spectral surveys of N_{1s}. (d) XPS spectral surveys of O_{1s}. (e) XPS spectral surveys of Ga_{3d}. (f) XPS spectral surveys of Ga_{2p}.

electronic characteristics of the prepared catalyst, both before and after the plasma reaction, we conducted XPS analysis on all the catalyst samples. A detailed spectrum survey of the XPS data is shown in Fig. 3b. It is important to note that the XPS investigations were performed *ex situ* to evaluate potential surface oxidation. Specifically, we subjected the Ir-4_f peak of the Ir/GaN to deconvolution using Gaussian components. As illustrated in Fig. 3b, the binding energy values of Ir-$4_{f5/2}$ and Ir-$4_{f7/2}$ for the fresh Ir/GaN catalyst (62.0 and 59.4 eV, respectively) exhibit negative shifts when compared to those of unsupported Ir nanoparticles, typically known to be at 63.8 and 61.8 eV.[39] This shift indicates an electron transfer from GaN to Ir, which is a consequence of electron-mediated surface interactions involving Ir, Ga, and N. Although the electronegativity of Ir (2.20)[40] is lower than that of N_{1s} (3.04) but higher than Ga (1.81),[41] the electron density in its proximity decreases. This reduced electron density induces an enhancement in binding energy, resulting in a negative shift in the peak position of the binding energy. This unequivocally illustrates the effective binding of Ir and GaN, establishing a robust interaction at the interfaces, which not only improves surface electrical properties but also facilitates the adsorption and catalytic upgrading of pyrolysis oil. A post-plasma reaction, a slight positive shift in comparison to the fresh Ir/GaN catalyst, was

observed. This could stem from amplified electron donation, charge transfer, or alterations in the local electronic environment due to interactions between the plasma and the catalyst. Essentially, these collaborative interactions between the plasma and the catalyst are anticipated to enhance the performance of oil upgrading processes. The peak observed at 397.5 eV originates from the presence of N_{1s} in GaN (Fig. 3c), and no other peaks corresponding to N–O interactions, such as the one at 400 eV, were identified. Furthermore, the electronic signal of O_{1s} (Fig. 3d) detected in both the initial and used Ir/GaN catalysts confirms the presence of gallium oxides, which aligns with the XRD findings mentioned earlier. The incorporation of Ir into the GaN structure led to a positive shift in the binding energy of Ga_{3d} (Fig. 3e) and Ga_{2p} (Fig. 3f), thereby, reinforcing our earlier hypothesis regarding electron donation, specifically Ga, to Ir and N. Subsequent to the plasma oil upgrading reaction, we observed additional positive shifts in the binding energies of Ga_{2p}, Ga_{3d}, and O_{1s}. These shifts could potentially arise from modifications in the local electronics given the plasma–catalyst interactions. It has been indicated that plasma can enhance the interaction between the catalyst and the support, resulting in better electron transfers.[42]

3.1.3. Catalyst morphology and dispersion. Our exploration of the dispersion of Ir atoms in nanocluster forms is concluded by the utilization of scanning transmission electron microscopy (STEM) in conjunction with energy-dispersive X-ray spectroscopy (EDX) characterization, as presented in Fig. 4. High-angle annular dark-field (HAADF) STEM images (Fig. 4a) unequivocally confirm the presence of clustered Ir atoms intricately arranged on the porous morphology of the GaN substrate. Evident from the yellow arrows in Fig. 4a and the HRTEM image (Fig. 4b), the size of the particles is measured below 2 nm. A meticulous particle size distribution analysis performed using ImageJ© reveals a mean size of approximately 1–1.5 nm for the clustered Ir atoms (Fig. 4c). The Ir, Ga, and N elemental mappings confirm their good distribution (Fig. 4d–f).

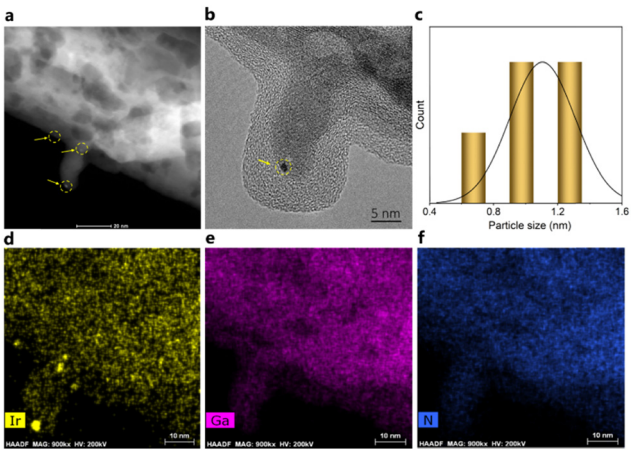

Fig. 4 (a) STEM-HAADF image of the fresh Ir/GaN catalyst. (b) HR-TEM image of the fresh Ir/GaN catalyst. (c) Particle size distribution of the Ir clusters on the GaN surface. (d) EDX mapping of Ir. (e) EDX mapping of Ga. (f) EDX mapping of N.

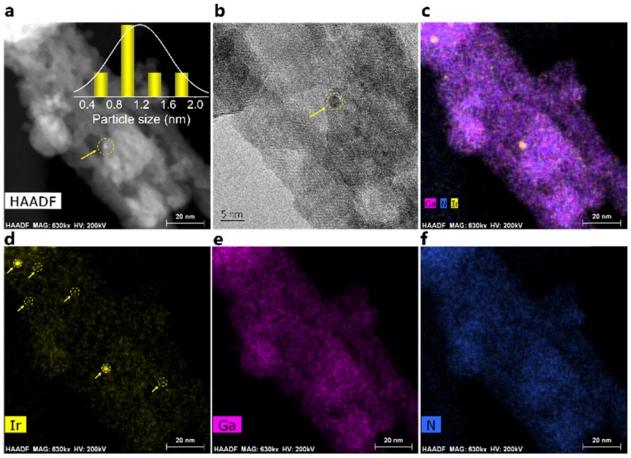

Fig. 5 (a) STEM-HAADF image of the spent Ir/GaN catalyst with the inset particle size distribution of the Ir clusters on the GaN surface. (b) HR-TEM image of the spent Ir/GaN catalyst. (c) EDX mapping images of all element overlapping. (d) EDX mapping of Ir. (e) EDX mapping of Ga. (f) EDX mapping of N.

A particle size of 0.6 nm for the Ir particles, as determined by CO pulsed chemisorption, falls within the particle distribution range inferred from TEM results. This insightful STEM-EDX investigation uncovers that the 2-methylimidazole ligand competes effectively, hindering undue crystal growth and agglomeration, as depicted in Fig. 1. This effect facilitates the formation of Ir atom clusters, suggesting novel synthetic pathways for efficient production of diverse metallic nanocluster catalysts. Remarkably, the STEM images also corroborate the approximate GaN pore size to be around 19 nm, a finding consistent with our prior N_2 adsorption/desorption measurements. Therefore, the presence of Ir atom clusters on the GaN surface significantly contributes to the observed amplification of the BET surface area, as this measurement encompasses an average of the highest Ir nanoclusters and the GaN substrate.

Furthermore, an investigation of the spent Ir/GaN catalyst by STEM-EDX (Fig. 5a) and HRTEM (Fig. 5b) unequivocally confirms the exceptional stability of the Ir/GaN catalyst. Notably, the clustered Ir atoms displays insignificant alteration during plasma reactions. These clusters persist, even exhibiting dimensions smaller than 1.5 nm in diameter, with certain regions measuring less than 1 nm (as indicated by the inset particle size distribution of Fig. 5a). Moreover, the Ir, Ga, and N elements maintain their good dispersion after the plasma reaction (Fig. 5c–f). At this juncture, these compelling observations lead us to hypothesize that Ir nanoclusters hold significant promise as catalysts for plasma-powered pyrolysis oil upgrading. The subsequent catalytic performance tests outlined in the forthcoming section are poised to provide a more comprehensive understanding of their activity, thereby substantiating this intriguing proposition.

3.2. Plasma catalysis driven pyrolysis oil upgrading performance

Inspired by the unique structural features of the Ir/GaN catalyst, we embark on an assessment of its intrinsic prowess

in pyrolysis upgrading. This evaluation is conducted alongside the empty Tube, pristine GaN, and Ir nanoclusters loaded on GaN, all under a continuous liquid mode configuration. In this operational setup, the liquid feed oil is introduced into the reactor upper section, while CH_4 is introduced into the plasma reaction zone from the reactor lower region. The liquid oil product is extracted from the upper-side portion of the reactor (Fig. S1, ESI†). Our primary objective in this context is to optimize mass transfer efficiency between the gaseous and liquid phases, thereby facilitating an enhanced upgrading performance. Control experiments were conducted to assess the influence of GaN and Ir/GaN catalysts on the pyrolysis upgrading process. The first set of control experiments involved plasma-powered CH_4 conversion under two conditions: one without feed oil, referred to as "Empty 1," and another with the presence of feed oil, referred to as "Empty 2" (Fig. 6a). The objective of these tests was to investigate the impact of feed oil on CH_4 conversion and H_2 formation. In the Empty 1 experiment, the CH_4 conversion rate was approximately 9.2%, and the H_2 yield reached around 77% at a flow rate of 100 cm^3 min^{-1} and a power input of 12 W. Interestingly, the introduction of feed oil into the reaction mixture in the Empty 2 experiment maintained the CH_4 conversion rate at around 9.1%. However, the H_2 yield decreased to 3.1%, while the total C_2–C_5 gas yield slightly increased from 17.2% (CH_4 only, Empty 1) to 2.1% (CH_4 with feed oil, Empty 2). This suggests that the generated H_2 was consumed in facilitating active H species for cleavage of pyrolysis oil molecules and stabilization of the formed cracking intermediates.[43] In the absence of oil, the plasma-mediated conversion of CH_4 resulted in a phenomenon known as methane liquefaction, leading to the formation of liquid products. However, the liquid yield from this reaction over the course of an hour remained relatively modest, measuring at 4.1%. Additionally, there was a coke yield of 1.7%. Notably, the predominant component in this process was gas, constituting 94.2% of the total gas products (H_2 and C_2–C_5) generated. This finding aligns with a similar observation reported by our research group in the liquefaction of methane under plasma conditions.[43] The presence of feed oil in the reaction with CH_4 (Empty 2 experiment) diminished gas to 5.3% but increases the liquid yield to 91.2%. It is worth mentioning that the introduction of GaN or Ir/GaN had limited impact on CH_4 conversion and upgraded the liquid oil yield, both remaining relatively stable at approximately 8.9% for CH_4 conversion and 86.0 and 86.8% for oil yields, respectively. However, the H_2 yield exhibited a decline to 4.8% for GaN and 4.5% for Ir/GaN. Additionally, a slight increase in the C_2–C_5 gas yield relative that of the Empty 2 test was observed from the upgrading reaction over the GaN and Ir/GaN catalyst, reaching approximately 3.4 and 3.2%, respectively. Therefore, it is reasonable to state that the liquid yield from pyrolysis oil upgrading in this study was not significantly affected by the liquid products of CH_4 liquefaction.

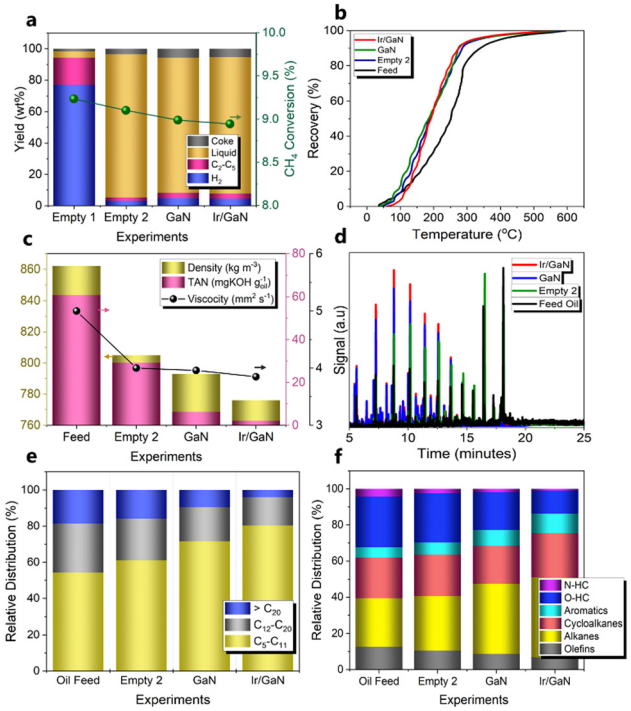

Fig. 6 (a) CH_4 conversion and product yields of experiments. (b) Boling curves of feed oil and upgraded oil produced from different plasma reactions. (c) Properties of feed oil and upgraded oil produced from different plasma reactions. (d) GC-MS spectra of the feed oil and upgraded oil produced from different plasma reactions. (e) Production distributions of feed oil and upgraded oil produced from different plasma reactions with gasoline components: C_5–C_{11}, diesel components: C_{12}–C_{20}, and heavy components: above C_{20}. (f) Hydrocarbon distribution of feed oil and upgraded oil. [Reaction conditions: CH_4 flowrate 100 cm^3 min^{-1}; feed oil flowrate: 0.05 cm^3 min^{-1}; catalyst weight: 0.1 g; plasma power: 12 W.]

The significance of catalysts became evident during the characterization of the upgraded liquid oil. The primary objective of upgrading pyrolysis oil to jet fuels is two-fold: to facilitate refining through advanced refinery technology rivalling conventional processes and to enhance the yield of higher-value light distillates. From the boiling curves shown in Fig. 6b, a lightening effect is clearly visible. Approximately 10% of the distillates from both the feed and upgraded oil in all experiments underwent initial distillation at around 100–122 °C. Subsequently, a significant portion, about 90%, was distilled within the range of 205–300 °C for the upgraded oil with the empty tube test (305 °C), GaN (287 °C), and the Ir/GaN catalyst (275 °C), whereas the feed oil required a higher distillation temperature of 340 °C. This suggests that about 10% of the distillates could be attributed to water-soluble compounds such as oxygenated hydrocarbons due to their similar boiling points. In contrast, the remaining part of the distillates (distilled at 205–252 °C) may serve as potential fuels, as their distillation temperatures are comparable to those of jet fuels (205–300 °C) and diesel (<343 °C).[44] The temperatures for 10% and 90% mass recovery of upgraded oil with the Ir/GaN in this work were 121 °C and 275 °C, respectively. While the maximum T10 temperature required for the aviation jet fuel is 205 °C, the real-time temperature for 90% mass recovery of the aviation fuel (T90) has not been reported.[4] However, it is worth noting that the T90–T10 ≥ 40 °C requirement, as specified in ASTM D7566,[45] has been met by the upgraded oil obtained in this

research. Additionally, the feed oil had a high-boiling distribution with an average molecular weight (MW) of 210 g mol^{-1} (Table S2, ESI†). However, after upgrading, all the boiling curves shifted towards lower-boiling distributions, indicating that the upgraded oil contained lighter hydrocarbons with lower boiling points than the feed oil. The oil resulting from the plasma reaction with Ir/GaN had the lowest average molecular weight of 165.6 g mol^{-1}, followed by GaN with an average molecular weight of 171.2 g mol^{-1}, and the upgraded oil from the empty tube (Empty 2 experiment) with an average molecular weight of 181.2 g mol^{-1}, in the increasing order. Such transformation of high-boiling compounds into low-boiling fractions caused a leftward shift in the boiling curve of the feed oil. This shift was brought about by the cracking of C–C bonds in the heavy components of feed oil.

In consistence with the reduction in the average molecular weight, other crucial properties including density, viscosity, and total acid number (TAN, derived from mg KOH consumed for titrating 1 g of oil) have also shown a reduction after treatment (Fig. 6c). For example, upgrading with the Empty Tube test reduced the density of the oil from 862 to 805 kg m^{-3} while with the presence of GaN and Ir/GaN, the densities were further diminished to 793 and 776 kg m^{-3}, respectively. These results met the standard density requirement for jet A-1 fuel, which should be between 775 and 840 kg m^{-3} (measured by ASTM D4052 at 15 °C).[46] The viscosity of the fuel significantly influences fuel injection, atomization, and combustion processes. Fig. 6c also presents the average viscosity values and their corresponding standard deviations for various distillates. Moreover, the viscosity also decreased from 5.00 mm^2 s^{-1} (feed oil) to 4.00, 3.96, and 3.85 mm^2 s^{-1} after upgrading with the empty tube (Empty 2 experiment), GaN, and Ir/GaN catalysts under plasma, respectively. While the viscosity of the oil upgraded through the plasma reaction over the Ir/GaN catalyst was still higher than the standard requirement for the jet fuel (ASTM D7042),[47] this work demonstrated significant improvements compared to conventional processes, even when using only a single model compound (α-tetralone), which achieved a viscosity of 3.94 mm^2 s^{-1} and a density of 927.8 kg m^{-3}.[48] This indicates the potential for further optimization for practical applications. Another critical parameter for the jet fuel is fuel acidity, with a maximum amount of 0.1 mg of KOH g_{oil}^{-1} (ASTM D3242).[49] The pyrolysis oil, due to the presence of various oxygenated compounds, often exhibits significant acidity, which can lead to corrosion issues, necessitating the use of specialized materials in engines and fuel feed systems. However, after upgrading with the empty tube, GaN, and Ir/GaN catalysts under the plasma regime, the TAN of the feed oil significantly decreased from 60.8 mg of KOH g_{oil}^{-1} to 29.2, 6.3, and 2.1 mg of KOH g_{oil}^{-1}, respectively. This nearly 30 times reduction in the acidity of the upgraded oil obtained over the plasma reaction with the Ir/GaN catalyst highlights its potential for further optimization. The insights gained from understanding the reaction mechanisms, discussed in the next section of this work, will be crucial for guiding future studies in this field.

Another crucial parameter of upgraded oils is their hydrocarbon product distribution characterized in detail to evaluate the upgrading efficiency and potential applications. First, Fig. S4 (ESI†) provides evidence for the alterations in the properties of the feed oil and the upgraded oil resulting from various experiments. The transition from the initial red-dark hue of the feed oil to a lighter yellow shade following the upgrading process with the empty tube, GaN, and Ir/GaN catalysts is clearly visible. Moreover, the GCMS signals of upgraded oils resulting from the plasma reaction using the empty tube, GaN, and Ir/GaN catalysts (Fig. 6d) exhibit a noticeable shift towards earlier retention times accompanied by a reduction in signal intensity under identical analysis conditions. This observation highlights substantial alterations in the composition of both the feed and upgraded oils. We thoughtfully integrated the GCMS results of the feed and upgraded oil, and we categorized the hydrocarbons present in both samples into three distinct groups: (1) gasoline components: C_5–C_{11}, (2) diesel components: C_{12}–C_{20}, and (3) heavy components: above C_{20}. The C_5 hydrocarbon listed here is cyclopentene as hexane (C_5H_{12}) evaporated strongly and quantified by micro-GC and listed in gas components, as shown in Fig. 6a. As presented in Fig. 6d, the feed oil contains 54.3% of C_5–C_{11}, 27.1% of C_{11}–C_{20}, and 18.6% of heavy component ($>C_{20}$). In the absence of the catalyst (Empty 2 experiment), the plasma upgrading led to an increase in gasoline components up to 61.0%, and decreases in diesel and heavy components to 23.1% and 15.9%, respectively. Incorporating GaN and Ir/GaN in the plasma zone significantly increased the gasoline components to 71.7% and 80.4%, respectively, while reducing the diesel components to 18.8% and 15.7%, respectively. Notably, Ir/GaN exhibited the highest reduction in heavy components, with only 4% detected in the upgraded oil, compared to 9.5% in the plasma upgrading with GaN. This shift from heavier hydrocarbons to lighter components, such as gasoline, which falls within the high-density jet fuel range, is crucial in producing the aviation fuel with improved properties, including lower freezing points and higher energy density, thus meeting stringent aviation requirements. As shown in Fig. 6f, the most hydrocarbons of feed oil are oxygenated compounds (O-HC) with 28.2%, followed by alkanes with 26.8% and cycloalkanes with 22.5%. Olefins occupy 16.7% while aromatic and nitrogen containing hydrocarbons (N-HC) occupy 5.6 and 4.2%, respectively. After upgrading with plasma in the absence of catalysts (Empty 2 experiment), a visible reduction in olefins to 10.6%, oxygenated compounds to 27.3%, and nitrogen-containing hydrocarbons to 2.4% was observed. In contrast, plasma led to slight increases in alkanes to approximately 30%, cycloalkanes to 23%, and aromatic to 6.8%. Commercial aviation fuels, for example Jet A-1 and Jet A, are widely used for international civil airline operations and within the US, respectively, making them the most prevalent aviation turbine fuels.[50] The composition of these jet fuels typically includes approximately 60% alkanes (comprising 20% alkane and 40% isoalkane), 20% cycloalkanes, and 20% aromatics in terms of volume fraction.[51] The relative proportions of these major

components may vary between other commercial jet fuels; nonetheless, alkanes, cyclohexane, and aromatic plays an important role for jet engines.[52] Aromatics have inferior combustion characteristics compared to alkanes, leading to elevated particulate emissions and lower specific energy. For jet engines, it is essential to have a certain number of aromatics to ensure appropriate swelling of elastomeric seals in the fuel systems, preventing leakage that could pose a fire safety hazard. Meanwhile, alkanes, particularly iso-alkanes, exhibit high specific energy, good thermal stability, and low freezing points.[53] Cycloalkanes complement iso-alkanes by offering similar benefits to aromatics, enabling fuels to meet density requirements and potentially providing seal-swelling capacity similar to that of aromatics.[54] Together, iso-alkanes and cycloalkanes have the potential to enhance fuels by providing high specific energy, increased energy density, and reduced emission characteristics. Due to their reactivity given by unsaturated bonds, olefins can lead to deposits in jet engines, making them unsuitable components for jet fuels. As a result, olefin content in jet fuel formulations is below 1%. The addition of GaN into the plasma regime boosts the content of alkanes, cycloalkanes, and aromatics to 38.6, 21.0, and 8.8%, respectively, while diminished olefins, oxygenated, and nitrogen-containing compounds to 8.8, 21.0 and 1.8%. Noticeably, plasma driven pyrolysis oil upgrading with the Ir/GaN lowers the nitrogen-containing, oxygenated, and olefin compounds to below 1.0, 12.7, and 6.8% while alkanes, cycloalkanes, and aromatics were increased to 44.2, 24.5, and 10.8%.

The distribution of these products closely resembles that of commercial jet fuels. It is important to highlight that conventional aviation fuels have only trace levels of oxygen contents;[45] however, the utilization of oxygenated biofuels in aviation remains a subject of scientific debate. Certain oxygenated compounds, such as antioxidants and stabilizers, enhance the fuel's stability, preventing degradation and reducing the formation of gums and deposits during storage, while also increasing its energy content. Additionally, certain oxygenates, like alkyl ethers, can boost the octane rating of the fuel, benefiting aviation engines with higher compression ratios and improving engine performance, while also contributing to reduced emissions of pollutants and potentially modifying the fuel's viscosity for better flow properties and handling characteristics.[55] This study also explored the impact of varying flowrates (0.05, 0.1, 0.15, and 0.2 cm^3 min^{-1}) on upgrading performance. Interestingly, an increase in the flow rate did not significantly alter the product yield, with the liquid yield improving from around 87% to 92%, coke yield reducing from 5.5% to 4.0%, and gas yield diminishing from 7.7% to 3.6% as the oil feed flow rate increased from 0.05 to 0.2% (Fig. S5, ESI†). Notably, the influence of the feed flow rate on upgrading performance became more apparent through the product distribution (Fig. S6, ESI†). Higher feed flow rates led to lower upgrading performance, evident, for instance, at 0.2 cm^3 min^{-1}, where N-HC reduced only from 4.2% (feed) to 3.0%, and O-HC declined from 28.2% (feed) to 26.2%. We attribute this trend to the suitability of the reactor size for lab-scale operations, suggesting that the utilization of high feed flow rates in this configuration is not optimal. While our primary focus is to provide novel insights into the activity of the Ir/GaN catalyst for plasma-driven biomass-derived pyrolysis oil to jet fuels, this research sets the stage for future work, including optimizing operational parameters, scaling-up studies, and conducting comprehensive techno-economic assessments.

3.3. Stability test

This work performed a 24 h stability test for plasma-driven pyrolysis oil upgrading using the Ir/GaN catalyst, with 8 h cycles of plasma on/off during each continuous reaction, mimicking the operational shifts of a practical industrial plant. Notably excelling in pyrolysis oil upgrading, the Ir/GaN catalyst demonstrates exceptional stability, maintaining nearly-consistent liquid product yields, CH_4 conversion, and properties even after 24 h of continuous operation (Fig. 7a). The distribution of products within the upgraded oil, collected at the 1 h, 8 h, 16 h, and 24 h marks of the plasma reaction, exhibits slight changes, as shown in Fig. 7b. While other distributions exhibit insignificant alterations, the most notable change is approximately 7.5% reduction in the distribution of oxygenated hydrocarbons (O-HC) from 12.7% at 1 h to 20.2% at 24 h. Nevertheless, this highlights comparative stability compared to thermal catalytic processes for hydrocarbon upgrading, typically reported within durations below 12 h (Table S3, ESI†). These findings affirm the outstanding stability of the catalyst, indicating that catalyst regeneration is presently unnecessary, considering the tradeoff between the intricacy of regeneration steps and the incremental improvement in catalytic performance. However, future research endeavors will involve extended stability tests over months or years with a larger scale to delve deeper into the potential for piloting the scaling up of this biomass-derived oil upgrading to the jet fuel process, building on the novel insights gained in catalyst development and performance from this study. A slight increment is observed in olefins, oxygenates, and nitrogen-containing products, reaching 10.9%, 16.0%, and 1.1%, respectively. This shift is accompanied by a reduction in alkanes, cycloalkanes, and aromatics, which decrease to 42.0%, 22.0%, and 8.0%,

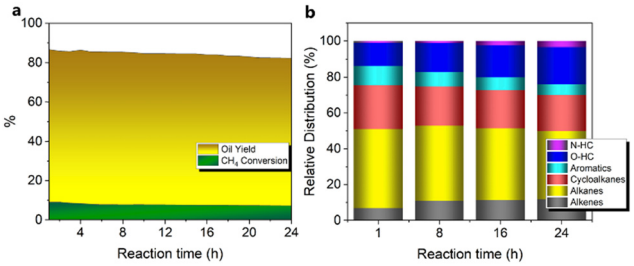

Fig. 7 (a) Stability test of the plasma driven pyrolysis oil with the nanocluster Ir/GaN catalyst over 24 h of a continuous reaction. (b) Hydrocarbon distribution of the upgraded oils at 1 h, 8 h, 16 h, and 24 h. [Reaction conditions: CH_4 flow rate 100 cm^3 min^{-1}; feed oil flow rate: 0.05 cm^3 min^{-1}; catalyst weight: 0.1 g; plasma power: 12 W].

respectively. The percentage of alkenes in our study still does not meet the current standards of commercial jet fuels. However, this pioneering work has unveiled novel avenues for future directions and offers a basis for further optimization efforts.

The TGA of the GaN and Ir/GaN catalysts spent over 8 h of the plasma reaction is shown in Fig. S7 (ESI†). As evident from the TGA profiles, the reduction in weight for the Ir/GaN catalyst is initiated within the temperature range of 300–350 °C and concludes at 550–600 °C with 13.5% followed by a gradual re-increase. Simultaneously, the TGA profile of the spent GaN sample exhibits a decline in mass starting around 100 °C and continuing until 500 °C with 14.2%, subsequently showing a lower degree of weight gain compared to that of the Ir/GaN catalyst. This reduction in weight within this specific temperature range could be attributed to the combustion of high molecular weight compounds originating from bio-oils, resulting from processes such as condensation and re-polymerization during the upgrading process, which become adsorbed on the catalyst structure and contribute to the formation of deposited coke. In the context of this study, the overall weight loss within this range is collectively referred to as deposited coke for the sake of simplicity. The subsequent increase in mass observed for the spent GaN and Ir/GaN catalysts could be attributed to the oxidation of Ga or Ir, leading to the formation of their respective oxides and resulting in a weight gain. In contrast to a thermal catalytic route for pyrolysis oil upgrading, which demonstrated a carbon deposition rate of 53.3% (using optimal CoMo supported on SBA-15 silica as an example),[56] the utilization of Ir/GaN in the plasma upgrading process exhibits a significantly lower rate of carbon deposition. The unique conditions created by non-thermal plasma, such as high-energy electrons and reactive species under near-ambient conditions, facilitate more efficient cracking and conversion of feedstock molecules, reducing the tendency for coke formation. This phenomenon is attributed to the ability of plasma to activate and break down complex hydrocarbons, preventing their accumulation on the catalyst surface, particularly on the nanocluster surface.

3.4. Unravelling the reaction pathways of plasma-induced methane activation and oil molecule upgrading

Compared to other catalytic upgrading methods of pyrolysis oil to jet fuels using batch-mode thermal catalytic processes (with copper-based catalysts) at 300 °C, which yield 10% cycloalkanes and oxygenated compounds higher than 14.2%,[57] the triphase plasma catalytic route employed in this study exhibits significantly better performance. Importantly, we have also observed promising results including better acidity, density, and viscosity properties, which warrant further investigation and exploration for large-scale applications. Despite this, the successful implementation of this technology for commercial purposes necessitates additional optimization and cannot be achieved without a comprehensive understanding of the underlying reaction mechanisms at a molecular level. We first characterized yielded plasma species fascinating insights into the

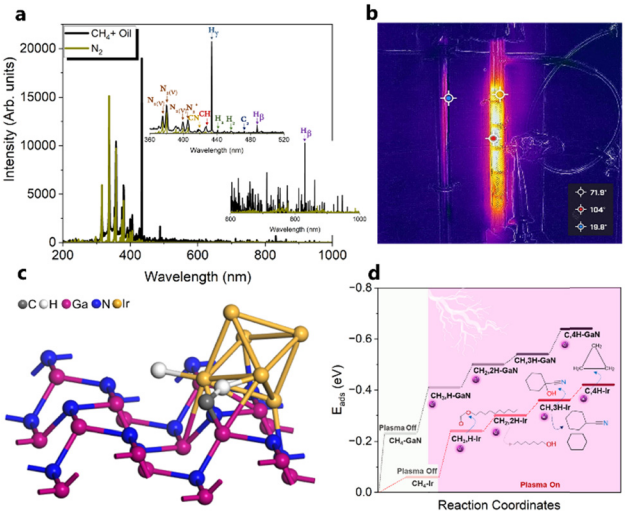

Fig. 8 (a) *In situ* OES spectra acquired during the plasma driven pyrolysis oil upgrading reaction with CH_4 over the Ir/GaN catalyst and N_2 spectra for subtracting the detected strong N_2 bands. (b) Temperature of the plasma reaction measured using an IR thermal camera. (c) Possible structure and adsorption of CH and H species on the Ir(110) nanoclusters supported on GaN. (d) Adsorption energy diagram and proposed reaction pathway of plasma driven pyrolysis oil upgrading with CH_4 using the Ir/GaN catalyst.

plasma-chemistry of the investigated mixture. Fig. 8a displays the recorded *in situ* OES spectra of the upgrading mixture (CH_4 + oil) and N_2. In this work, the OES of N_2 plasma was recorded to subtract strong N_2 bands detected during the pyrolysis oil upgrading reaction from N-containing products. The *in situ* OES spectra of the upgrading reaction reveal prominent bands associated with the excited CH, C_2, H_γ, H_β, H_2, and CN species, which differentiate from the N_2 OES bands showing only nitrogen plasma species peaks. The CH band peaking at 430 nm can be attributed to $A^2\Delta \rightarrow X^2\Pi$. The peak at 422 nm of CN species was assigned to the $B_2\Sigma \rightarrow X^2\Sigma$ energy level transitions. The most intense peak of the OES profile at 434 nm belongs to the $5d^2D \rightarrow 2p^2p^\circ$ of H_γ while H_β with $4d^2D \rightarrow 2p^2p^\circ$ energy level transitions was detected at 488 and 831 nm. The H_2 bands at 441 and 456 nm attribute to the $G^1\Sigma_g^+ \rightarrow G^1\Sigma_u^+$. The C_2 band captured at 473 nm belongs to $d^3\Pi_8 \rightarrow a^3\Pi_u$. These energy level transitions are consistent with those in other research studies.[58–60] Oxygen-related bands were not detected due to factors such as the weaker intensity of its emission lines relative to strong N_2, H_2, CH, and CN species in the oil and gas system and potential interferences from these compounds and radicals. The strong signal of H radicals during the plasma reactions initially took us falling into two scenarios: (i) H from CH_4 dissociation and (ii) cleavage from oil molecules. Nonetheless, control experiments, as depicted in Fig. 6a above, show insignificant impact of oil on hydrogen formation and CH_4 conversion. We hence conclude that the dominant presence of active H species in the plasma reactor originate from CH_4 as a primary source and intermediates from dehydrogenation of pyrolysis oil molecules as a second source. In this manner, the counter flow of CH_4 and oil facilitates the rapid transfer of

H from gas–liquid interface to the fluidized GaN and Ir/GaN surface, contributing to catalytic oil upgrading reactions. This explains for the better upgrading performance from catalytic tests relative to the Empty experiments. In this work, the IR thermal camera indicated the temperature of the plasma reactor was around 100 ± 5 °C (Fig. 8b). As we mentioned earlier, the control experiment, conducted with an external thermal heater set at 100 ± 5 °C, revealed no CH_4 conversions or improvements in oil properties, demonstrating the effective mitigation of conventional thermal factors' influence on the upgrading performance. The ''thermal effects'' of plasma, on the other hand, have long been overshadowed, given the characterization of plasma as non-thermal, with seemingly unchanged outlet gas and liquid temperatures. However, these thermal influences predominantly arise from interactions among the constituents of the gaseous, liquid, and catalyst medium within the reactor. The voltage–current profile depicting the gas (CH_4)–liquid (oil)–solid (catalyst) system exhibits micro-pulsed plasma discharges, highlighting intricate interactions between the plasma and the reaction medium within the reactor (Fig. S8, ESI†). This results in a conversion of a fraction of the discharge power into thermal energy, thereby raising the catalyst and surrounding temperatures. These interactions involve inelastic collisions between high-energy electrons and substantial particles, leading to the release of energy by the formation of excited molecules and ionized atoms. Additionally, collisions between ions, neutral particles, and free electrons contribute further to the energy release. The presence of thermal effects cannot be disregarded, especially at the catalyst surface, where nanoclusters play a crucial role in promoting the upgrading reaction. We posit that while these thermal effects may not exhibit characteristics akin to traditional thermal catalytic processes due to their relatively moderate nature,[61] they do play a significant role. Specifically, these effects contribute to promoting the desorption rate of adsorbed species on the catalyst surface. This, in turn, helps mitigate surface poisoning, ultimately leading to an enhanced upgrading performance. In addition to considering hydrogen (H), another crucial factor to take into account is the presence of active CH_x species. These species play a significant role in lowering the activation energy required for the cleavage of C–H, C–N, and C–O bonds within the non-aqueous plasma environment. The sequential dehydrogenation reaction of CH_4 initiates with the detachment of a single hydrogen atom from the CH_4 molecule, progressing through transitional species to ultimately form C ($CH_4 \rightarrow CH_3 \rightarrow CH_2 \rightarrow CH \rightarrow C$), with hydrogen being released at each step. In the final dehydrogenation stage, the most stable form of carbon (C) is produced, predominantly in the coke form, which does not significantly contribute to the cleavage of pyrolysis molecules. In contrast, our upgrading performance results, demonstrating a reduction in the molecular weight of upgraded oil compared to the feed oil, suggest that CH_3 and CH_2 are less likely to undergo oligomerization with other hydrocarbons in the oil, leading to the formation of heavier products. Instead, CH_x species, along with H, are expected to play a dominant role in reacting with oil molecules. We propose the adsorption of CH_x and H, originating from CH_4 dissociation on the Ir(100) surface, as shown in Fig. 8c. Our DFT calculations (Fig. 8d and Table S4, ESI†) reveal that the adsorption energy of CH_4 on GaN is −0.23 eV and that on Ir is −0.06 eV. Under plasma conditions, the adsorption energies of transitional species, including CH_3, CH_2, CH, and C, on the GaN(110) surface, with the proposed adsorption geometry depicted in Fig. S9 (ESI†), are −0.41, −0.5, −0.54, and 0.64 (Table S4, ESI†), respectively. These corresponding values obtained from the Ir(100) surface were −0.24, −0.3, −0.36, and −0.42 eV. Plasma augmentation enhances surface properties, promoting stronger molecule adsorption on the catalyst surface. Referring to the aforementioned XPS results, we observe a positive energy binding shift in the Ir/GaN comparison following the plasma reaction, indicating higher electron density in the surroundings under plasma conditions, leading to stronger molecule binding. When considering the GaN and Ir/GaN surfaces, the GaN surface exhibits stronger binding with CH_4 and active species such as CH and H. Consequently, it displays higher dehydrogenation barriers, where site poisoning becomes the limiting factor rather than CH_4 activation, resulting in lesser rate enhancements. Conversely, the Ir/GaN catalyst exhibits more substantial rate enhancements due to its weaker binding of CH_4 and active species, enabling Ir to be the active surface that bind species weakly for catalytic reactions. This correlation between adsorption energy and reaction performance is consistent with findings in plasma-powered ammonia production.[62]

The exploration of the potential for H* and CH_x^* production from CH_4 in the plasma was conducted to generate the necessary active species for the hydrodeoxygenation and cleavage of unsaturated hydrocarbons reactions. These reactions specifically target oxygen-containing compounds and olefins present in the feed chemical structure. Within the active volume of the plasma discharge reactor, a multitude of energetic species, including electrons, highly reactive species H* and CH_x*, and metastable forms, engage in collisions with feed oil molecules. These collisions induce excitation or the generation of products through energy transfer. Consequently, compared to conventional thermal reactors, the mechanism of reactions in a plasma reactor is more intricate. Proposing a singular mechanism to explain the reaction pathways in the plasma reactor is challenging, even several studies[63–65] used simpler model compounds to verify it. Nonetheless, integrating thermodynamic species databases with plasma discharge mechanisms allows us to suggest the primary reaction steps. Whereby, taking an oxygen contained-compound of $C_xH_yOCH_3$ in the feed for an example, the excitation of this molecule to higher energy levels occurs due to collisions with high-energy electrons or temporarily excited collision partners such as H* and CH_x*. The chemical bonds of $C_xH_yOCH_3$ can be dissociated through collisions with high-energy electrons or temporarily excited collision partners such as H* and CH_x*, and highly energetic electrons, resulting in decomposition of $C_xH_yOCH_3$ to C_xH_yOH and then C_xH_y. This possible pathway coincides with other research studies.[66]

The comprehensive Techno-Economic Assessment (TEA) of NTP-driven pyrolysis oil to jet fuels falls outside the scope of the current work. Instead, our focus is on reporting the catalytic performance of nanoclustered Ir supported on GaN in a triphase plasma system. This marks the first instance of such an investigation, emphasizing the novelty of our research in this specific catalytic context. However, we performed a thoughtful comparison with other works in the literature, which upgraded the model compound of pyrolysis oil to jet fuels by thermal catalytic processes and also with other plasma process (Table S3, ESI†). The NTP process featured from the thermal catalytic one by its atmospheric pressure while thermal ones were operated at high pressures (8–120 bars) and much lower temperatures while thermal one run with higher than 350 °C. In our prior research,[67] we conducted a thorough TEA that focused on evaluating the cost-effectiveness of renewable diesel production *via* CH_4-assisted waste cooking oil. This was proposed as an alternative to the traditional pure H_2 hydrotreating methods. Our findings indicate that utilizing CH_4 in the hydrotreating process is significantly more cost-effective than using H_2. Specifically, the production cost of the CH_4-assisted catalytic process was determined to be $0.365 per kg of renewable diesel. In comparison, the cost of H_2 was $0.574 per kg for renewable diesel and biodiesel. Building on these findings and considering similar observations in plasma-assisted heavy oil upgrading with CH_4,[23,68–70] we are confident in asserting that the economic benefits of plasma-driven CH_4 treating pyrolysis oil are substantial for future jet fuel production. This confidence is based on the elimination of an additional step involving pure H_2—a process often derived from energy-intensive and highly endothermic natural gas reforming.[71] Consequently, we anticipate that plasma-driven pyrolysis oil with CH_4 will emerge as a promising and sustainable approach for the production of premium fuels and chemicals even from heavy oils.

4. Conclusions

This work showcases a highly efficient H_2-free process for pyrolysis oil upgrading using a triphase plasma catalytic system. Our experimental findings highlight impressive upgraded oil yields, approximately 87%, with the density and viscosity meeting the ASTM standards. Notably, the product distribution, including alkanes, cycloalkanes, and aromatics, aligns closely with requirements for commercial jet fuels. These remarkable results were achieved under mild operating conditions, with temperatures hovering around 100 °C and at ambient pressure. By harnessing the potent capabilities of cleavage reactions for long C–H bonds of plasma, we facilitated the effective transfer of active H and CH_x species derived from CH_4 to the oil liquid, primarily driven by highly energetic electrons. Our computational analysis supports the notion that nanoclustered Ir, with its weaker binding to CH_4 and active species, coupled with the thermal effects on the Ir cluster surface, accelerates the desorption of adsorbed species. This dynamic interplay promotes rapid upgrading reactions, significantly lowering the barriers for cleaving C–H, C–N, and C–O bonds. As a result, pyrolysis oil can be efficiently upgraded to gasoline, all while operating under mild conditions. The implications of our findings lay the groundwork for scaling up and optimization, not only within central oil and gas plants but also in fostering regional economic growth. This work has the potential to stimulate the emergence of new jet fuel production technology, spanning from biomass feedstock cultivation and pyrolysis technology development to fuel production. The positive socio-economic effects are particularly promising for rural areas rich in biomass resources. By taking this leap forward, this work contributes to the more conscientious and energy-efficient future, signifying a significant stride toward the aviation industry's aspirations for a greener and more responsible path.

Author contributions

Hoang M. Nguyen: methodology, investigation, formal analysis, writing – original draft, and data curation. Ali Omidkar: simulation. Wenping Li: visualization. Zhaofei Li: formal analysis and data curation. Hua Song: conceptualization, supervision, validation, and writing – review and editing.

Conflicts of interest

There are no conflicts to declare.

Acknowledgements

The TEM-EDX analysis in this work used the 4D LABS core facility at Simon Fraser University (SFU) supported by the Canada Foundation for Innovation (CFI), the British Columbia Knowledge Development Fund (BCKDF), and the Pacific Economic Development Canada (PacifiCan).

References

1 L. Zhang, T. L. Butler and B. Yang, *Recent trends, opportunities and challenges of sustainable aviation fuel*, John Wiley & Sons, Inc., 2020.
2 S. Arrowsmith, *Directive Article*, 2020, **30**, 1–184.
3 R. Sacchi, V. Becattini, P. Gabrielli, B. Cox, A. Dirnaichner, C. Bauer and M. Mazzotti, *Nat. Commun.*, 2023, **14**, 3989.
4 P. Lahijani, M. Mohammadi, A. R. Mohamed, F. Ismail, K. T. Lee and G. Amini, *Energy Convers. Manage.*, 2022, **268**, 115956.
5 R.-X. Chen and W.-C. Wang, *Renewable Energy*, 2019, **135**, 819–835.
6 W.-T. Chen, Y. Zhang, T. H. Lee, Z. Wu, B. Si, C.-F. F. Lee, A. Lin and B. K. Sharma, *Nat. Sustainability*, 2018, **1**, 702–710.
7 X. Cui, X. Zhao and D. Liu, *Green Chem.*, 2018, **20**, 2018–2026.

8 C. J. Wrasman, A. N. Wilson, O. D. Mante, K. Iisa, A. Dutta, M. S. Talmadge, D. C. Dayton, S. Uppili, M. J. Watson, X. Xu, M. B. Griffin, C. Mukarakate, J. A. Schaidle and M. R. Nimlos, *Nat. Catal.*, 2023, **6**, 563–573.
9 W. Liu, W. You, W. Sun, W. Yang, A. Korde, Y. Gong and Y. Deng, *Nat. Energy*, 2020, **5**, 759–767.
10 H. Wang, J. Male and Y. Wang, *ACS Catal.*, 2013, **3**, 1047–1070.
11 J. S. Wright and K. U. Ingold, *J. Chem. Educ.*, 2000, **77**, 1062.
12 A. H. Zacher, D. C. Elliott, M. V. Olarte, H. Wang, S. B. Jones and P. A. Meyer, *Biomass Bioenergy*, 2019, **125**, 151–168.
13 N. O. Burov, V. D. Savelenko, M. A. Ershov, A. O. Vikhritskaya, E. O. Tikhomirova, N. A. Klimov, V. M. Kapustin, E. A. Chernysheva, A. V. Sereda and T. M. Abdellatief, *Renewable Energy*, 2023, **215**, 118898.
14 A. Eschenbacher, T. Myrstad, N. Bech, H. D. Thi, M. Auersvald, K. M. Van Geem and A. D. Jensen, *Fuel*, 2021, **302**, 121198.
15 T. S. Ahamed, S. Anto, T. Mathimani, K. Brindhadevi and A. Pugazhendhi, *Fuel*, 2021, **287**, 119329.
16 H. M. Nguyen, A. Omidkar and H. Song, *ChemPlusChem*, 2023, **88**, e202300129.
17 H. M. Nguyen, C. M. Phan, G. H. Pham, Y. Asakuma, R. Vagnoni and S. Liu, *J. Ind. Eng. Chem.*, 2021, **94**, 173–179.
18 H. M. Nguyen, F. Gorky, S. Guthrie and M. L. Carreon, *Catal. Today*, 2023, **418**, 114141.
19 H. M. Nguyen, A. Omidkar, W. Li, S. Meng, Z. Li and H. Song, *Chem. Eng. J.*, 2023, **471**, 144748.
20 H. M. Nguyen and M. L. Carreon, *ACS Sustainable Chem. Eng.*, 2022, **10**, 9480–9491.
21 D. Mei, X. Zhu, C. Wu, B. Ashford, P. T. Williams and X. Tu, *Appl. Catal., B*, 2016, **182**, 525–532.
22 Y. Zheng, Q. Ruan, J. Ren, X. Guo, Y. Zhou, B. Zhou, Q. Xu, Q. Fu, S. Wang and Y. Huang, *Appl. Catal., B*, 2023, **323**, 122170.
23 S. Meng, W. Li, H. Xu, Z. Li, Y. Li, J. Jarvis and H. Song, *Appl. Catal., B*, 2021, **297**, 120459.
24 S. Meng, A. Wang, P. He and H. Song, *J. Phys. Chem. Lett.*, 2020, **11**, 3877–3881.
25 Y. Wang, W. Yang, S. Xu, S. Zhao, G. Chen, A. Weidenkaff, C. Hardacre, X. Fan, J. Huang and X. Tu, *J. Am. Chem. Soc.*, 2022, **144**, 12020–12031.
26 C. Liu, J. Kang, Z.-Q. Huang, Y.-H. Song, Y.-S. Xiao, J. Song, J.-X. He, C.-R. Chang, H.-Q. Ge, Y. Wang, Z.-T. Liu and Z.-W. Liu, *Nat. Commun.*, 2021, **12**, 2305.
27 M. G. Kibria, F. A. Chowdhury, S. Zhao, B. AlOtaibi, M. L. Trudeau, H. Guo and Z. Mi, *Nat. Commun.*, 2015, **6**, 6797.
28 K. Trangwachirachai, A. L. Huang, H. K. Chen, C. L. Chen, J. F. Lee, H. K. Tian and Y. C. Lin, *Mater. Today Chem.*, 2023, **30**, 101500.
29 Z. Lu, V. Cherepakhin, T. Kapenstein and T. J. Williams, *ACS Sustainable Chem. Eng.*, 2018, **6**, 5749–5753.
30 M. Tang, S. Mao, X. Li, C. Chen, M. Li and Y. Wang, *Green Chem.*, 2017, **19**, 1766–1774.
31 E.-J. Kim, J. Shin, J. Bak, S. J. Lee, K. H. Kim, D. Song, J. Roh, Y. Lee, H. Kim, K.-S. Lee and E. Cho, *Appl. Catal., B*, 2021, **280**, 119433.
32 Y.-X. Dai, W.-L. Xin, L.-H. Xu, J. Li, Y.-X. Li, J. Li, S. Cosnier, X.-J. Zhang, R. S. Marks and D. Shan, *Appl. Surf. Sci.*, 2022, **591**, 153066.
33 T. Shao, P. Zhang, L. Jin and Z. Li, *Appl. Catal., B*, 2013, **142–143**, 654–661.
34 Q. Wang, C.-Q. Xu, W. Liu, S.-F. Hung, H. Bin Yang, J. Gao, W. Cai, H. M. Chen, J. Li and B. Liu, *Nat. Commun.*, 2020, **11**, 4246.
35 M. Farrag, *Microporous Mesoporous Mater.*, 2018, **257**, 110–117.
36 E. C. Neyts, K. Ostrikov, M. K. Sunkara and A. Bogaerts, *Chem. Rev.*, 2015, **115**, 13408–13446.
37 H. Xu, Z. Li, Y. Li and H. Song, *Commun. Chem.*, 2021, **4**, 152.
38 C. Dong, C. Lian, S. Hu, Z. Deng, J. Gong, M. Li, H. Liu, M. Xing and J. Zhang, *Nat. Commun.*, 2018, **9**, 1252.
39 V. Pfeifer, T. Jones, J. V. Vélez, C. Massué, M. Greiner, R. Arrigo, D. Teschner, F. Girgsdies, M. Scherzer and J. Allan, *Phys. Chem. Chem. Phys.*, 2016, **18**, 2292–2296.
40 M. Kim, H. Kang, E. Hwang, Y. Park, W. Jeong, Y. J. Hwang and D.-H. Ha, *Appl. Surf. Sci.*, 2023, **612**, 155862.
41 J. C. Boeyens, *Z. Naturforsch., B: J. Chem. Sci.*, 2008, **63**, 199–209.
42 Z. Ye, L. Zhao, A. Nikiforov, J.-M. Giraudon, Y. Chen, J. Wang and X. Tu, *Adv. Colloid Interface Sci.*, 2022, **308**, 102755.
43 S. Meng, W. Li, Z. Li and H. Song, *Catal. Sci. Technol.*, 2023, **13**, 4665–4672.
44 A. ASTM, *Annual Book of ASTM Standards*, 2015.
45 A. Standard, *ASTM International*, West Conshohocken, PA, 2013.
46 A. Standard, *2011 ASTM Annual Book of Standards*, 2018.
47 D. ASTM, *ASTM International*, West Conshohocken, PA, USA, 2016.
48 G. Vijayakumar and A. Pandurangan, *Energy*, 2017, **140**, 1158–1172.
49 E. S. K. Why, H. C. Ong, H. V. Lee, W.-H. Chen, N. Asikin-Mijan and M. Varman, *Energy Convers. Manage.*, 2021, **243**, 114311.
50 H. Zhang, Y. Fang, M. Wang, L. Appels and Y. Deng, *J. Environ. Manage.*, 2020, **274**, 111214.
51 Z.-H. Jin, J.-T. Chen, S.-B. Song, D.-X. Tian, J.-Z. Yang and Z.-Y. Tian, *Combust. Flame*, 2021, **226**, 190–199.
52 Z. Yang, K. Qian, X. Zhang, H. Lei, C. Xin, Y. Zhang, M. Qian and E. Villota, *Energy*, 2018, **154**, 289–297.
53 R. C. Striebich, L. M. Shafer, R. K. Adams, Z. J. West, M. J. DeWitt and S. Zabarnick, *Energy Fuels*, 2014, **28**, 5696–5706.
54 P. Kallio, A. Pásztor, M. K. Akhtar and P. R. Jones, *Curr. Opin. Biotechnol*, 2014, **26**, 50–55.
55 M. D. Boot, M. Tian, E. J. Hensen and S. M. Sarathy, *Prog. Energy Combust. Sci.*, 2017, **60**, 1–25.
56 S. Ahmadi, Z. Yuan, S. Rohani and C. Xu, *Catal. Today*, 2016, **269**, 182–194.
57 X. Kong, C. Liu, Y. Fan, M. Li and R. Xiao, *ACS Sustainable Chem. Eng.*, 2023, **11**, 7454–7465.

58 Z. Fan, H. Sun, S. Zhang, W. Han, C. Zhang, Q. Yang and T. Shao, *Chem. Eng. J.*, 2022, **436**, 135190.
59 G. Wattieaux, M. Yousfi and N. Merbahi, *Spectrochim. Acta, Part B*, 2013, **89**, 66–76.
60 K. Clay, S. Speakman, G. Amaratunga and S. Silva, *J. Appl. Phys.*, 1996, **79**, 7227–7233.
61 G. Giammaria, G. van Rooij and L. Lefferts, *Catalysts*, 2019, **9**, 185.
62 P. Mehta, P. Barboun, F. A. Herrera, J. Kim, P. Rumbach, D. B. Go, J. C. Hicks and W. F. Schneider, *Nat. Catal.*, 2018, **1**, 269–275.
63 Y. Liu, L. Dou, R. Zhou, H. Sun, Z. Fan, C. Zhang, K. K. Ostrikov and T. Shao, *Energy Convers. Manage.*, 2021, **250**, 114896.
64 L. Wang, Y. Yang, J. Sun, Y. Xin, X. Zhu and B. Sun, *J. Anal. Appl. Pyrolysis*, 2023, **170**, 105931.
65 H. Taghvaei, M. B. Hosseinzadeh, S. Rezazadeh, M. R. Rahimpour and A. Shariati, *Chem. Eng. J.*, 2015, **281**, 227–235.
66 M. A. Mudassir, M. Batool, S. Kousar, M. A. Makarem, E. T. Razia, M. Meshksar, M. Murtaza, K. Tariq, M. A. Ud Din, M. A. Bodlah and M. R. Rahimpour, *Fuel Process. Technol.*, 2023, **250**, 107872.
67 A. Omidkar, H. Xu, Z. Li, K. Haddadian and H. Song, *J. Cleaner Prod.*, 2023, **414**, 137512.
68 H. Xu, Y. Song, Y. Zhang and H. Song, *Fuel*, 2022, **309**, 122155.
69 M. Gharibi, A. Khosravi, M. R. Khani, S. S. Shahabi, E. D. Guy and B. Shokri, *J. Electrost.*, 2015, **76**, 178–187.
70 M. J. Gallagher, R. Geiger, A. Polevich, A. Rabinovich, A. Gutsol and A. Fridman, *Fuel*, 2010, **89**, 1187–1192.
71 A. Alagumalai and H. Song, *Biofuel Res. J.*, 2023, **10**, 1966–1973.